Theoret. Comput. Fluid Dynamics (1998) 11: 305–322

Theoretical and Computational Fluid Dynamics

Instability of an Axisymmetric Vortex in a Stably Stratified, Rotating Environment

W.D. Smyth

College of Oceanography and Atmospheric Sciences,
Oregon State University, Corvallis, OR 97331, U.S.A.

J.C. McWilliams

National Center for Atmospheric Research Boulder, CO 80307, U.S.A.
and
Atmospheric Sciences Department, Institute of Geophysics and Planetary Physics, UCLA,
Los Angeles, CA 90095, U.S.A.

Communicated by J.R. Herring

Received 6 December 1996 and accepted 1 November 1997

Abstract. We investigate the stability of a barotropic vorticity monopole whose stream function is a Gaussian function of the radial coordinate. The model is based on the inviscid Boussinesq equations. The vortex is assumed to exist on an f-plane, in an environment with constant, stable density stratification. In the unstratified, nonrotating case, we find growth rates that increase monotonically with increasing vertical wave number, the so-called "ultraviolet catastrophe" characteristic of symmetric instability. This type of instability leads to rapid turbulent collapse of the vortex, possibly accompanied by wave radiation. In the limit of strong background stratification and rotation, the vortex exhibits a scale-selective instability which leads to the formation of stable lenses. The transition between these two regimes is sharp, and coincides approximately with the centrifugal stability boundary.

1. Introduction

Visualizations of numerically simulated Navier–Stokes turbulence have shown that such flows are dominated by coherent vorticity concentrations in the form of tubes and sheets (e.g., Vincent and Meneguzzi, 1991). The simplest models for such structures, the *line vortex* and the *sheet vortex*, have been studied for over a century now. Knowledge of the characteristic evolutionary patterns of these elementary flow structures is now proving invaluable in understanding the mechanics of turbulence. Line and sheet vortices appear at all scales (an expression of the self-similar character of turbulence), and they often play the role of the large, energy-containing motions whose instability drives the downscale cascade. Continuous versions of these elementary structures, namely, the axisymmetric vortex and the parallel shear layer, provide useful models for flows which arise commonly in both engineering and geophysical contexts, and have been the object of intensive study over several decades.

In the geophysical context, it is important that we take account of the effects of planetary rotation and density stratification. Interest in rotating, stratified turbulence has been energized in the past decade by evidence that large-scale geophysical flows are driven in part by an upscale cascade of energy from motions

forced at smaller scales (e.g., Gage and Nastrom, 1986), a process which depends crucially on the interaction of stratification and rotation effects (e.g., Bartello, 1995).

Axisymmetric vortices have served as models for hurricanes, tropical cyclones, and tornadoes. However, the majority of the work in this area has been done in the engineering community, where stratification and rotation effects are less important. As a result, the impacts of these geophysical factors on vortex evolution have only recently begun to be explored (Gent and McWilliams, 1986; Flatau and Stevens, 1989; Willoughby, 1988; Peng and Williams, 1991; Gill *et al.* 1993; Weber and Smith, 1993, Gill and Sneddon; 1995). In each of these studies, one of several reduced physical models was employed (the hydrostatic approximation, shallow-water equations, the quasi-geostrophic model, or the barotropic vorticity equation). In the present work, we extend the results of those studies using the full Boussinesq equations.

A factor which has complicated the study of axisymmetric vortices, even in the absence of stratification and rotation, is the lack of any counterpart to Squire's theorem. That result guarantees that the primary instability of a parallel shear flow will be two-dimensional, i.e., it will not vary in the direction parallel to the original vorticity, regardless of the precise form of the shear flow. In contrast, the primary instability of a vortex can be either two-dimensional (external) or three-dimensional (internal), depending on the details of the vortex shape. This distinction can be quite crucial. In the case of hurricanes, for example, external modes can determine a storm's trajectory (Willoughby, 1990), whereas internal modes have no such influence.

A crucial issue is the manner in which the stability characteristics of a given vortex depend on the strength of the background rotation (f) and stratification (N). Gent and McWilliams (1986, hereafter GM86) have shown that, in the quasigeostrophic (QG) limit of large f and N, vortices generally exhibit *scale-selective* instability, i.e., instability over a finite range of length scales, with a well-defined fastest-growing mode. In contrast, the symmetric instability displayed by vortices in unstratified, nonrotating regimes exhibits *ultraviolet catastrophe* (UVC) (e.g., Smyth and Peltier, 1994), i.e., the region of instability extends to infinite wave numbers (ignoring viscosity), and the growth rate grows monotonically, so there is no fastest-growing mode.

This distinction between balanced and unbalanced behavior is illustrated in Figure 1. In the first case, the absolute value of the Rossby number is 2, which is certainly not $\ll 1$, but the qualitative predictions of QG theory appear to hold, i.e., we observe an adjustment to a balanced state consisting of stable lenses with the aspect ratio near $|f/N|$. Such structures are commonly observed in the ocean (e.g., McWilliams, 1985). In the second case, the absolute Rossby number is increased to 8, and the adjustment process does not occur. Instead, the vortex suffers a rapid turbulent collapse.

How does this change from UVC to balanced behavior occur? Does the infinite regime of instability become finite with the introduction of nonzero f and N, then shrink gradually as those parameters become large? On the contrary, our results suggest that there is a well-defined boundary on the (f, N) plane across which the change in behavior occurs, i.e., that the change is a "catastrophe" in the mathematical sense. Another way to phrase this issue is to ask "How fast can a vortex rotate and still obey the QG approximation, at least qualitatively?" The answer appears to be that QG theory is valid over a surprisingly large region of parameter space, but there is a distinct boundary whose crossing has dramatic results.

This is a theoretical study of the inviscid linear instability of a localized (i.e., with zero total circulation), monopolar, barotropic vortex that has what previous studies indicate is a typical velocity profile in this regard. Our goal here is to be comprehensive in the regimes of rotation and stratification, which are pervasive geophysical influences. We do not consider either viscosity, which would ultimately limit the UVC, or advective nonlinearity, which presumably would become important following the unstable growth of initially weak disturbances. We do not attempt to match the circumstances of any particular class of real geophysical vortices. The relevant equations are derived in Section 2. Section 3 contains the bulk of the results, beginning with the simple case of no background stratification or rotation (Section 3a). We then investigate the separate effects of nonzero stratification and rotation (Sections 3b and 3c, respectively). In Section 3d we consider the combined effects of stratification and rotation, including the QG limit which was the focus of GM86. Our results are summarized in Section 4.

2. Mathematical Preliminaries

In this section, we derive the relevant model equations and describe the numerical methods used in their solution (Section 2a). We then display the perturbation kinetic energy budget, which is used to diagnose

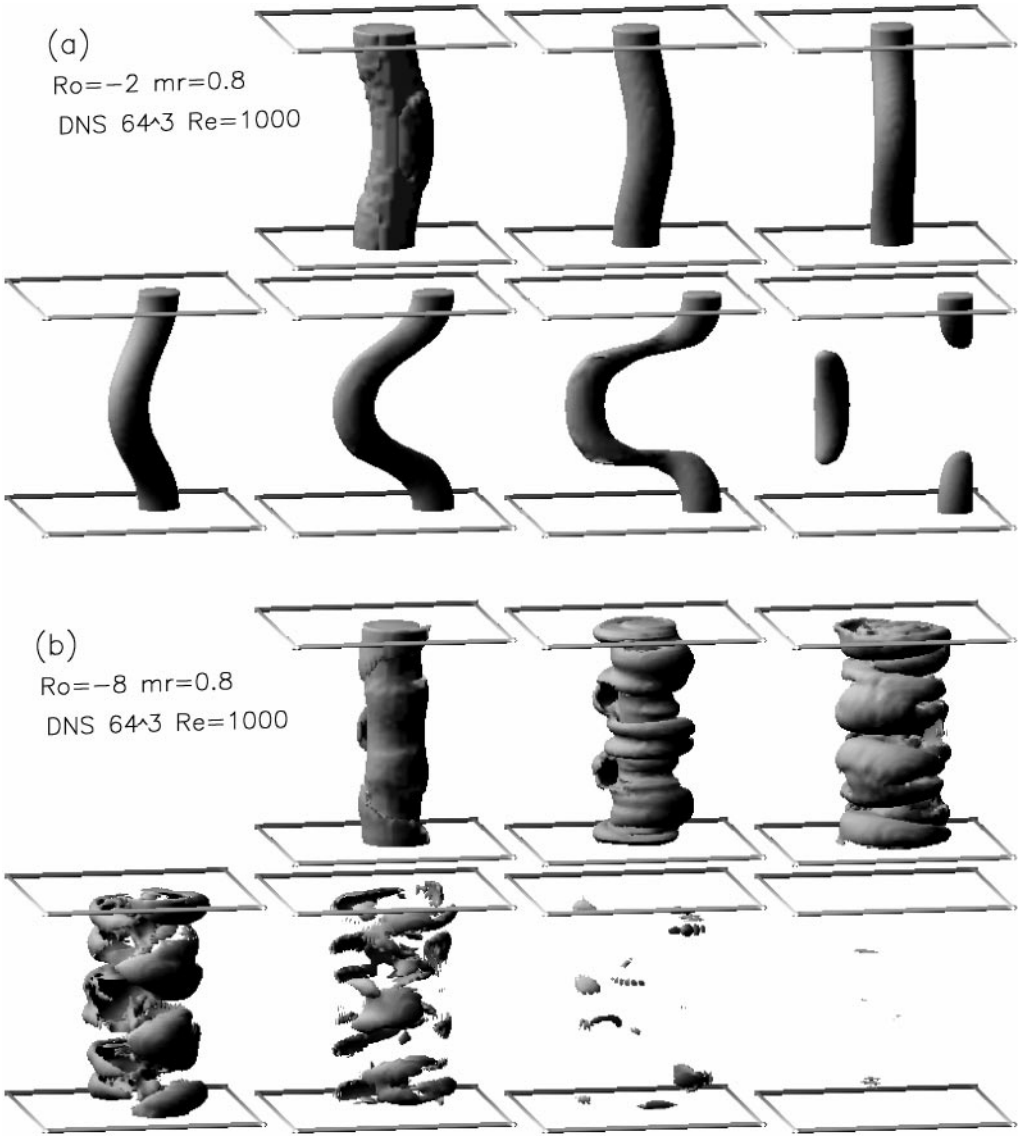

Figure 1. Direct numerical simulations of unstable, barotropic cyclones. The model is nonhydrostatic and Boussinesq. Boundary conditions are periodic in the horizontal, and free-slip and insulating in the vertical. The array size is 64^3. The Reynolds number, based on vortex radius and maximum velocity, is 1000. The evolution of an enstrophy isosurface is shown; the interval between successive frames is ten turnaround times. The two cases differ only in the ambient rotation and stratification. In each case, $|f/N| = 1$. In case 1 ($Ro = -2$), an unstable oscillatory mode causes the vortex to bend, and ultimately break into stable lenses with the aspect ratio near $|f/N|$. (This mode is described in detail in Figure 14(a) and the accompanying discussion.) In case 2, the initial conditions are identical, except that f and N are reduced by a factor of four to give $Ro = -8$. In this case, turbulent motions appear at all resolved scales, and the vortex is destroyed.

the mechanism of instability (Section 2b). In Section 2c we describe the particular vorticity profile that is employed in these investigations, and in Section 2d we discuss the implications of Rayleigh's centrifugal instability criterion for the present case.

2a. The Model Equations

Our mathematical model is based on the equations of motion for an incompressible, inviscid, nondiffusive, Boussinesq fluid on the f-plane. In terms of cylindrical coordinates $\{r, \theta, z\}$ (which represent the radial, azimuthal, and vertical directions, respectively) and corresponding velocity components $\{u, v, w\}$,

the equations read

$$\frac{Du}{Dt} - fv - \frac{v^2}{r} = -\frac{\partial \pi}{\partial r}, \tag{1a}$$

$$\frac{Dv}{Dt} + fu + \frac{uv}{r} = -\frac{1}{r}\frac{\partial \pi}{\partial \theta}, \tag{1b}$$

$$\frac{Dw}{Dt} = -\rho^* g - \frac{\partial \pi}{\partial z}, \tag{1c}$$

$$\frac{D\rho^*}{Dt} = 0, \tag{1d}$$

$$\frac{1}{r}\frac{\partial}{\partial r} ru + \frac{1}{r}\frac{\partial v}{\partial \theta} + \frac{\partial w}{\partial z} = 0m \tag{1e}$$

where ρ^* represents the relative departure of the density ρ from a state of constant density $\overline{\rho}$, i.e., $\rho = \overline{\rho}(1+\rho^*)$, π represents $\overline{\rho}^{-1}$ times the departure of the pressure from the corresponding hydrostatic state: $p = \overline{p} - \overline{\rho} g z + \overline{\rho}\pi$, and g is the gravitational acceleration. The material derivative is defined by

$$\frac{D}{Dt} \equiv \frac{\partial}{\partial t} + u\frac{\partial}{\partial r} + \frac{v}{r}\frac{\partial}{\partial \theta} + w\frac{\partial}{\partial z}.$$

This system possesses steady solutions of the form

$$u = 0, \qquad v = V(r), \qquad w = 0, \qquad \pi = \pi_0(r, z), \qquad \rho^* = \rho_o(z), \tag{2a}$$

which obey conditions of gradient and hydrostatic balance, viz:

$$\frac{\partial \pi_0}{\partial r} = fV + \frac{V^2}{r}, \qquad \frac{\partial \pi_0}{\partial z} = -g\rho_o. \tag{2b}$$

In this paper we are concerned with the behavior of infinitesimal perturbations to the steady flows described by (2). Accordingly, we linearize (1) about (2) and obtain

$$\frac{D_0 u'}{Dt} - (2\Omega + f)v' = -\frac{\partial \pi'}{\partial r}, \tag{3a}$$

$$\frac{D_0 v'}{Dt} + (Z + f)u' = -\frac{1}{r}\frac{\partial \pi'}{\partial \theta}, \tag{3b}$$

$$\frac{D_0 w'}{Dt} = -N^2 h' - \frac{\partial \pi'}{\partial z}, \tag{3c}$$

$$\frac{D_0 h'}{Dt} = w', \tag{3d}$$

$$\frac{1}{r}\frac{\partial}{\partial r} ru' + \frac{1}{r}\frac{\partial v'}{\partial \theta} + \frac{\partial w'}{\partial z} = 0, \tag{3e}$$

where the material derivative associated with the background flow is

$$\frac{D_0}{Dt} = \frac{\partial}{\partial t} + \Omega\frac{\partial}{\partial \theta}$$

and primes denote perturbation quantities.

$$\Omega = \frac{V}{r} \quad \text{and} \quad Z = \frac{1}{r}\frac{\partial}{\partial r} rV \tag{4}$$

represent the background angular velocity and relative vorticity, respectively.

$$h' = -\frac{\rho'}{d\rho_0/dz} \quad \text{and} \quad N^2 = -\frac{g}{\rho_0}\frac{d\rho_0}{dz}$$

are the vertical displacement and the squared buoyancy frequency, respectively. We only consider cases in which $N^2 > 0$, and it is understood that N represents the positive square root of N^2. The problem is separable if the hydrostatic approximation is made (i.e., setting the left-hand side of (3c) to zero), or if N^2 is assumed to be constant. For the present calculations, we make the latter assumption.

With N^2 constant, perturbations may be assumed to have the normal mode form

$$\varphi'(r,\theta,z,t) = \hat{\varphi}(r)e^{i(l\theta+mz-\omega t)}, \tag{5}$$

in which φ represents any perturbation quantity and only the real part is physically relevant. l and m are azimuthal and vertical wave numbers, and ω is the complex angular frequency. (For maximum generality, we have assumed that the vertical domain is infinite. Inclusion of upper and lower boundary conditions is straightforward.) After substituting (5) into (3), we combine (3a–d) to obtain the following polarization relations:

$$(\Phi_a - \sigma^2)\hat{u} = i\sigma\hat{\pi}' - \frac{il}{r}(2\Omega + f)\hat{\pi}, \tag{6a}$$

$$(\Phi_a - \sigma^2)\hat{v} = (Z + f)\hat{\pi}' - \frac{\sigma l}{r}\hat{\pi}, \tag{6b}$$

$$\hat{w} = \frac{m\sigma\hat{\pi}}{\sigma^2 - N^2}, \tag{6c}$$

$$\hat{h} = \frac{im\hat{\pi}}{\sigma^2 - N^2}, \tag{6d}$$

in which $\sigma = \omega - l\Omega$ is the Doppler-shifted frequency. Primes now represent differentiation with respect to r.

$$\Phi_a(r) = (2\Omega + f)(Z + f) \tag{7}$$

is the absolute centrifugal stability. We now substitute (6) into (3e) to obtain a single ordinary differential equation for $\hat{\pi}$, namely,

$$\left(\frac{r\hat{\pi}'}{\Phi_a - \sigma^2}\right)' + \left[-\frac{l}{\sigma}\left(\frac{2\Omega + f}{\Phi_a - \sigma^2}\right)' - \frac{l^2}{r(\Phi_a - \sigma^2)} + \frac{m^2 r}{\sigma^2 - N^2}\right]\hat{\pi} = 0. \tag{8}$$

The boundary condition for the limit $r \to 0$ is obtained by matching to the asymptotic solution:

$$\hat{\pi} \sim r^l. \tag{9}$$

For the outer boundary condition, a solid boundary may be imposed at any radius r by requiring that $u = 0$ at the boundary or, using (6a),

$$\sigma\hat{\pi}' = \frac{l}{r}(2\Omega + f)\hat{\pi}.$$

An alternative, which we employ in the present study, is to impose a condition of outgoing radiation at some large radius by matching to the asymptotic solution:

$$\hat{\pi} = \begin{cases} r^{-l} & \text{if m = 0;} \\ H_l^{(n)}(\kappa r) & \text{otherwise,} \end{cases} \tag{10}$$

which is valid in the limit $r \to \infty$. In (10) the radial scale factor κ is given by

$$\kappa^2 = m^2\frac{\sigma^2 - f^2}{N^2 - \sigma^2}, \tag{11}$$

and $H_l^{(n)}$ represents the lth order Hankel function of type n. When $\mathrm{Im}(\omega) \neq 0$, i.e., for a growing disturbance, we choose $n = 1$. When $\mathrm{Im}(\omega) = 0$, i.e., for a wavelike disturbance, we choose $n = 1$ (resp. $n = 2$) when the quantity $\omega(\omega^2 - f^2)$ is positive (resp. negative). If the matching is done at a sufficiently large radius ($|\kappa r| \gg 1$), the asymptotic form of the Hankel function may be used to obtain the simpler boundary condition

used, for example, in GM86:

$$\hat{\pi}' = \begin{cases} -\dfrac{l}{r}\hat{\pi} & \text{if m = 0;} \\ (3-2n)i\kappa\hat{\pi} & \text{otherwise.} \end{cases} \tag{12}$$

In practice, we find that the condition ($|\kappa r| \gg 1$) can be overly restrictive, so we employ the more accurate form (10). In deriving the outer boundary conditions, we have assumed that the circulation of the vortex is zero. For the case of nonvanishing circulation, (12) is valid, but (10) must be modified.

Several common approximations may be obtained as special cases of (8). The barotropic vorticity equation (e.g., Weber and Smith, 1993) is equivalent to (8) with the vertical wave number m set to zero. The hydrostatic approximation (e.g., Flatau and Stevens, 1989) may be applied by replacing $\sigma^2 - N^2$ with $-N^2$ in the rightmost term. If, in addition to assuming that $\sigma^2 \ll N^2$, one assumes that σ, Ω, and Z are all much smaller than f, the quasi-geostrophic potential vorticity equation (e.g., GM86) results.

Equation (8), together with the boundary conditions (9), constitutes an eigenvalue problem whose solution implicitly defines the dispersion relation for normal mode perturbations, namely,

$$\omega = \omega(l, m, f, N) \tag{13}$$

pertaining to a given vorticity profile. To investigate (13), we solve the eigenvalue problem associated with (8) using a multiple shooting method similar to that employed by Hazel (1972). Starting from the asymptotic solutions (9) evaluated at small and large r, we integrate inward to an intermediate radius r_0. Continuity of the solution and its derivative require that the matching function

$$M(\omega; l, m, f, N) = \hat{\pi}'_-\hat{\pi}_+ - \hat{\pi}'_+\hat{\pi}_-$$

vanish. The subscripts + and $-$ in the above equation refer to limits taken as r approaches r_0 from larger and from smaller values, respectively (see Hazel (1972) or Smyth and Peltier (1989) for further details of the shooting method). A standard root-finding algorithm is employed to search the complex ω-plane for zeros of M. Double precision arithmetic is used throughout the computation. As our primary interest is in unstable modes, we have made no provision for bypassing singularities; as a result, stability boundaries are not computed exactly. Although there is the possibility of multiple families of unstable modes, we examine only the fastest-growing mode at each point in the (l, m, f, N) parameter space, in order to achieve broad coverage in a feasible number of computations.

2b. The Perturbation Kinetic Energy Budget

A useful diagnostic is the perturbation kinetic energy equation

$$\frac{\partial}{\partial t}\langle K' \rangle = -r\frac{d\Omega}{dr}\langle u'v' \rangle - N^2\langle w'h' \rangle - \frac{\partial}{\partial r}\langle u'\pi' \rangle \tag{14}$$

in which $K' = (u'^2 + v'^2 + w'^2)/2$ and

$$\langle\ \rangle = \int_0^{2\pi} r\ d\theta \int_0^{2\pi/m} dz \tag{15}$$

represents the volume average over one vertical wavelength (assuming $m \neq 0$). Equation (14) reveals that the background rotation f has no effect on the perturbation energy, since the Coriolis force is directed perpendicular to the motion. The energy for disturbance growth may come either from the kinetic energy of the background vortex or from the potential energy associated with the density stratification. These energy sources are described by the first and second terms, respectively, appearing on the right-hand side of (14). The flows to be considered in this paper are all stably (or neutrally) stratified, so that the buoyancy term in (14) constitutes an energy sink; the shear production term acts alone to supply energy to growing disturbances. The third term on the right-hand side of (14) is the radial divergence of the radial energy flux. For all of the eigenmodes to be described in this paper, (14) is satisfied to within $\sim 0.1\%$.

2c. Background Profiles

The investigations reported here focus on the stability characteristics of a particular columnar vortex, that whose streamfunction has the Gaussian form

$$\psi = \exp\left(-\left(\frac{r}{\bar{r}}\right)^2\right), \tag{16}$$

in which $\bar{r}$ is a constant. This profile is commonly employed as a model of an isolated, axisymmetric vortex, and was employed in GM86 as the "standard" case. Profiles of the associated velocity, angular velocity, vorticity, and centrifugal stability for this vortex are shown in Figure 2. Results for a range of alternative vortex profiles will be reported separately.

We explore the stability characteristics of the vortex (16) under a range of values of background stratification (N) and rotation (f). We assume that $N^2 \geq 0$ and $N \geq 0$; f is allowed to take either sign. Alternatively, we may describe background stratification and rotation in terms of the Froude number

$$Fr = \frac{m}{N}\bar{Z}\bar{r} \tag{17}$$

and the Rossby number

$$Ro = \frac{\bar{Z}}{f}. \tag{18}$$

In these expressions, $\bar{r}$ is the radial length scale and $\bar{Z}$ is the inverse time scale, equal to the maximum of the absolute background vorticity $|Z|$. For the present case, $\bar{r} = 1$ and $\bar{Z} = 4$. Note that a reversal in the sign of f is equivalent to a reversal of the sense of the rotation. Since the core vorticity is negative (Figure 2(b)), we refer to cases of negative f (or Ro) as "cyclonic" and to cases of positive f (or Ro) as "anticyclonic."

2d. Centrifugal Instability

Rayleigh's centrifugal instability theorem (e.g., Drazin and Reid, 1981) applies to the case of an axisymmetric disturbance ($l = 0$) of a baroclinic vortex in a nonrotating, unstratified environment ($f = N = 0$) with a rigid boundary at some r. The theorem effectively places an upper bound on the growth rate:

$$\omega_i^2 \leq -\min_r \Phi, \tag{19}$$

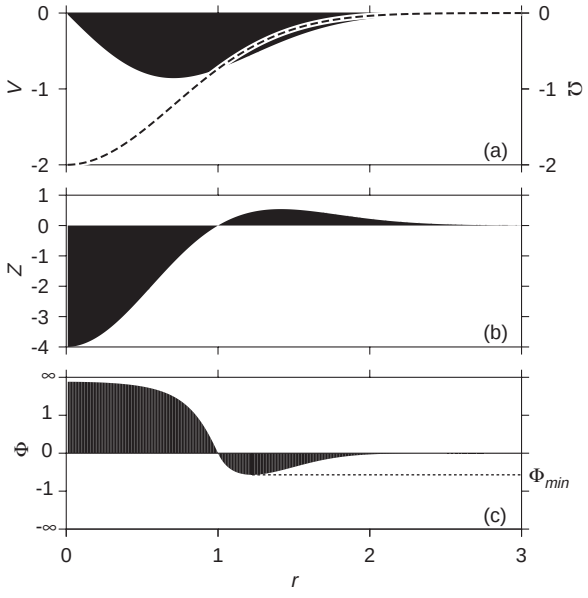

Figure 2. Radial dependence of the background vortex. (a) Filled curve: background tangential velocity $V(r)$; dashed curve: angular velocity $\Omega(r)$. (b) Background vorticity $Z(r)$. (c) Centrifugal stability $\Phi(r)$, equivalent to Φ_a for the case $f = 0$. The vertical axis is stretched to magnify values near zero via the scaling $y = \Phi/(1+|\Phi|)$. The global minimum $\Phi_{\min}$ is minus the square of the largest growth rate permitted by Rayleigh's theorem (Section 2d).

where $\Phi(r) = 2\Omega Z$ is the centrifugal stability function. The usefulness of (19) in the present work is limited by several factors: nonzero f, nonzero N, nonzero l, and the radiation boundary condition. We now discuss those limitations in turn.

The theorem is extended to cover the rotating case ($f \neq 0$) by replacing Φ with Φ_a (Kloosterzeil and van Heijst, 1991). The inclusion of stable stratification ($N > 0$) does not change the result at all. This is not surprising, since (19) is an upper bound, and stable stratification tends to reduce instability. The proof does not hold for the case of an infinite domain with a radiation boundary condition (12), but we expect that the radiation condition, like stable stratification, will usually act to damp instability, and is thus unlikely to invalidate (19). The remaining assumption, i.e., $l = 0$, would appear to be the most restrictive. Note, however, that the effect of setting $l = 0$ in (8) is similar to the result of taking the limit $m \to \infty$. This suggests that, even for non axisymmetric modes, (19) may provide a boundary on the domain in which UVC occurs. We know of no rigorous proof for this, but we will show that the proposition holds for the particular vortex profile considered here.

We now identify the stability boundaries implied by Rayleigh's theorem for the particular case (16). The condition for instability is that Φ_a be negative for some range of r. Thus, we need to find the zeros of Φ_a, which may be zeros of $2\Omega + f$ and/or zeros of $Z + f$ (7). In the present case, there are at most two such points:

- If $Ro < -e^2$, $2\Omega + f$ is negative definite, but $Z + f$ has two roots, which lie on either side of $r = \sqrt{2}$. Φ_a is negative between those radii.
- If $-e^2 < Ro < 1$, Φ_a is positive definite.
- If $Ro > 1$, $Z + f$ has a root in the range $r < 1$, and $2\Omega + f$ has a root at $r = \sqrt{\ln Ro} > 1$. Φ_a is negative between those radii.

Thus, nonzero growth rates are expected outside the range $-e^2 < Ro < 1$.

3. Results

We have set ourselves the task of exploring solutions of (8) and (9) in the four-dimensional parameter space defined by the wave numbers l and m and by the geophysical parameters f and N. Our strategy is to choose particular cuts through the (f, N) plane, and for each cut to explore the whole range of values of l and m at which unstable modes appear. We begin in Section 3a with a look at the unstratified, nonrotating case, $f = N = 0$. We then examine the effects of stratification alone ($f = 0$; $N > 0$) in Section 3b, and the effects of rotation alone ($N = 0$, $f \neq 0$) in Section 3c. In Section 3d we investigate the combined effects of rotation and stratification. We focus on two cases: the simple case in which $f = N$, and the more geophysically relevant case in which $f/N = 10^{-2}$.

3a. The Unstratified, Nonrotating Case

In the unstratified, nonrotating case, instability is found at three azimuthal wave numbers only: $l = 0$, $l = 1$, and $l = 2$. Figure 3 shows growth rates (ω_i) and frequencies (ω_r) as functions of the vertical wave number m. The $l = 0$ mode is stationary ($\omega_r = 0$), while the $l = 1$ and $l = 2$ modes are oscillatory.

In the case of parallel flow, the existence of a "critical" surface (on which the Doppler-shifted frequency vanishes) is a necessary condition for instability. An analogous result holds in the present case; each unstable mode possesses at least one radius r_c at which $\omega_r - l\Omega(r_c) = 0$ (in the axisymmetric case $l = 0$, this condition is satisfied trivially). Critical radii tend to be located just outside the radius $r = 1$ at which Φ becomes negative (Figure 2(c)). As a result, ω_r and l tend to be roughly proportional, as is evident in Figure 3. Throughout this study, we will find that $l = 0$ modes are stationary, while the frequencies of modes with $l \neq 0$ increase with increasing l.

In the unstratified, nonrotating case illustrated in Figure 3, the $l = 0$, $l = 1$, and $l = 2$ modes are all internal (i.e., their growth rates are maximized at nonzero vertical wave number), and only the $l = 2$ mode is unstable at $m = 0$. Each mode exhibits a semi-infinite bandwidth, with ω_i increasing monotonically in the limit of

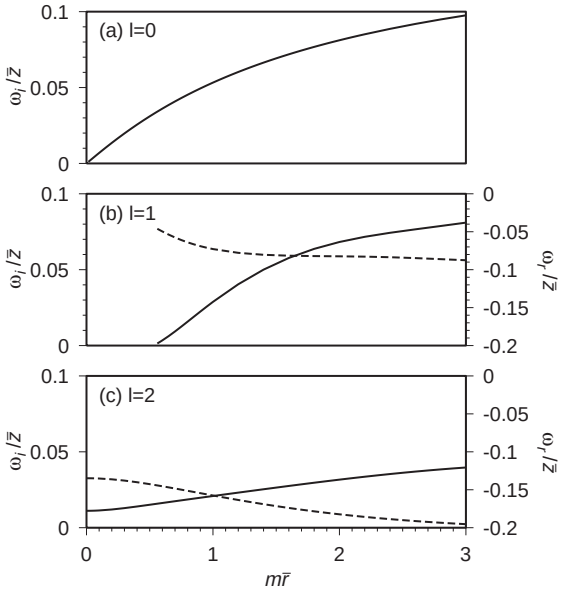

Figure 3. Growth rates (solid curves) and frequencies (dashed curves) versus vertical wave number for the unstratified, nonrotating case. (a) l = 0; (b) l = 1; (c) l = 2.

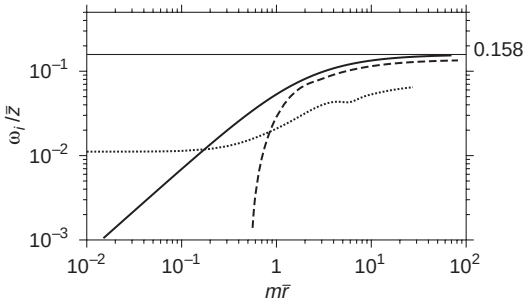

Figure 4. Growth rate versus vertical wave number for the l = 0 (solid), l = 1 (dashed), and l = 2 (dotted) cases. Background rotation and stratification are zero. The thin horizontal line marks the maximum growth rate of centrifugal instability as predicted by Rayleigh's theorem (cf. Figure 2(c)).

large vertical wave number, i.e., the UVC mode of instability described in the Introduction. In a viscous fluid, we expect to see a transfer of energy directly from the mean flow into the dissipation subrange. This result is illustrated further in Figure 4, where $\omega_i(m)$ is plotted on logarithmic axes. While growth rates generally increase monotonically with m, they cannot increase without bound because of (19). The horizontal line on figure 4 indicates the maximum growth rate permitted by (19). Growth rates of the axisymmetric modes seem to asymptote to this value as m is increased, while nonaxisymmetric modes attain smaller growth rates.

Figure 5 shows the radial structures of the l = 0, l = 1, and l = 2 modes at m = 2. The curves represent the terms in the disturbance kinetic energy equation (14). Because N = 0, the buoyancy term vanishes. Amplification due to the shear production term tends to be maximized near the critical radius. In each case,

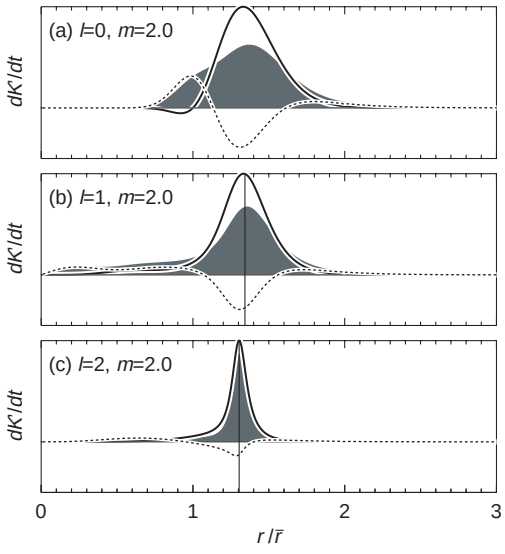

Figure 5. Terms in the perturbation kinetic energy budget (14) for selected unstable modes in the unstratified, nonrotating case. The filled curve is the left-hand side of (14), $2\omega_i\langle K'\rangle$. The thick solid curve represents the shear production term, and the dashed curve is the convergence of the radial energy flux. Units on the vertical axis are arbitrary, but the same for all curves. Vertical lines indicate critical radii.

the radial energy flux transports energy away from this region. The radial energy flux is directed primarily inward. For the l = 0 mode, energy is deposited just inside the band in which production occurs. In the l = 1 case, energy is spread over a wider region extending to the axis of the vortex. The radial energy flux is markedly weaker for the l = 2 mode than for the other two cases.

3b. The Effects of Stratification

In this set of calculations, we set f = 0 and increase N from near zero to large positive values (or decrease the Froude number to zero). The results given in the previous section correspond to the limit $Fr \to \infty$. As in the unstratified, nonrotating case, instability is found only at azimuthal wave numbers 0, 1, and 2. The effect of decreasing Fr on the growth rates of these modes is illustrated in Figure 6. Not surprisingly, the growth rate usually decreases with decreasing Fr. The effect is seen first at large m, where a given value of Fr corresponds to a relatively high value of N.

The l = 0 mode (Figure 6(a)) remains stationary in the presence of stratification. At low Froude numbers, its growth rate becomes independent of m, i.e., it becomes a function of Fr only. The l = 0 mode is stabilized when Fr decreases below a critical value, that value being approximately 14 for all m. Thus,

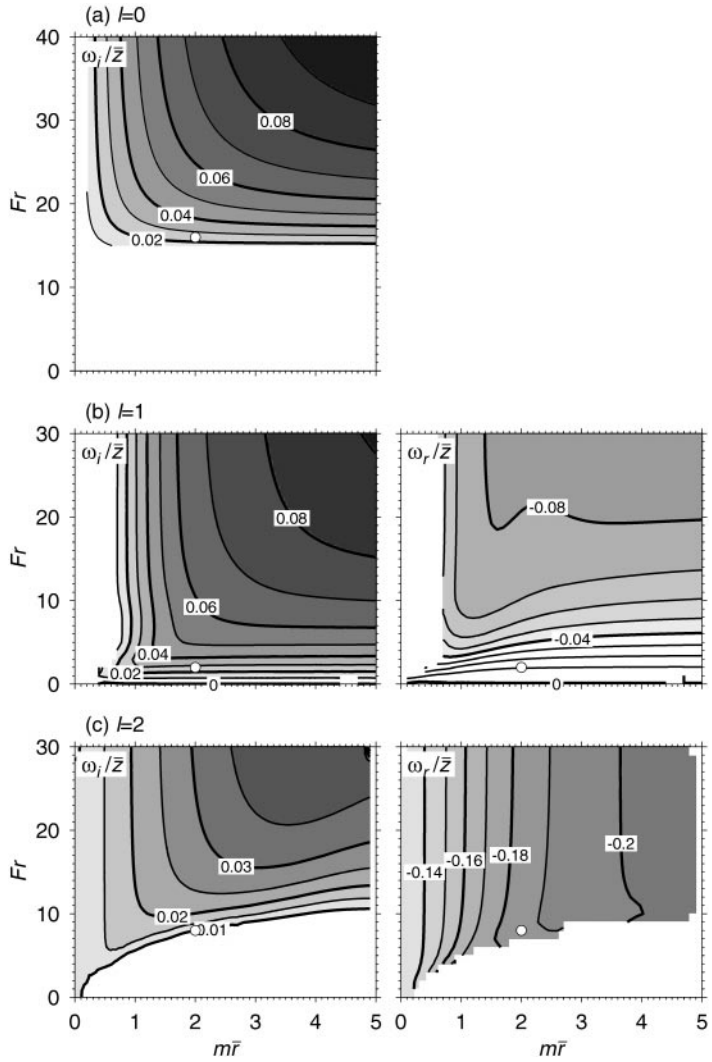

Figure 6. Growth rate versus vertical wave number and Froude number for the stratified case. Azimuthal wave numbers are (a) l = 0, (b) l = 1, and (c) l = 2. The limit $Fr \to \infty$ corresponds to Figure 3. White circles indicate the modes illustrated in Figure 7.

however strong the stratification may be, the flow is unstable to axisymmetric modes for sufficiently large m, and the minimum wave number for instability is proportional to N.

The $l = 1$ mode (Figure 6(b)) responds to increasing stratification in much the same manner as does the $l = 0$ mode, with two exceptions. First, the stability boundary is located at or very close to $Fr = 0$ for all m, so that instability in strongly stratified regimes extends to larger vertical wavelengths than is the case for axisymmetric modes. Second, modes with small m, which are stable in the unstratified case, are *destabilized* at low Froude numbers. We therefore see that "stable" stratification can actually have a destabilizing influence on columnar vortices, an effect which will be seen to be crucial in the quasi-geostrophic regime. The oscillation frequency, like the growth rate, becomes a function of Fr only as $Fr \to 0$.

The $l = 2$ mode (Figure 6(c)) is unstable for all m in the limit $Fr \to \infty$ (cf. Figures 2(c) and 3). For Fr less than about 10, high vertical wave numbers are stabilized, while modes near $m = 0$ remain unstable. (Note that external modes are unaffected by stratification.) As Fr is decreased, the oscillation frequency remains a function of m, in contrast to the $l = 1$ case (cf. right-hand frames of Figure 5(b) and 5(c)). To summarize, the fastest-growing mode is found at $l = 1$ and $m \to \infty$ for all Fr, except in the limit $Fr \to 0$. In that limit, only the external $l = 2$ mode is unstable.

Figure 7 shows the spatial structures of selected $l = 0$, $l = 1$, and $l = 2$ modes at $m = 2$ in the presence of stratification. These eigenfunctions may be compared with the corresponding results from the unstratified case, which are displayed in Figure 5. In each case illustrated we have chosen Fr to be close to the stability boundary, so that stratification effects will be readily apparent.

An obvious difference from the unstratified case is the reduced tendency for disturbance energy to be focused near the critical radius. In the $l = 1$ case, the mode shown is in the region of very small Fr in which oscillation frequency is decreasing rapidly to zero (cf. Figure 6(b)), i.e., critical radii are moving to large r, despite the fact that the shear needed for energy production is near $r = 1$. In the $l = 2$ cases, production is focused near the critical radius, but the radial energy flux is so strong that disturbance energy is spread evenly over a wide band of radii.

Because N is nonzero, the damping effects of the buoyancy term are significant. Bouyancy tends to stabilize regions in which energy is deposited by the radial flux. This effect is dominant in the $l = 0$ case, but is less pronounced in the $l = 1$ case, so that the inward energy flux maintains disturbance energy nearly to the vortex center.

This $l = 2$ mode exhibits a more pronounced tendency to radiate energy outward from the critical radius. We now examine the physics of this radiating mode in detail. In the spirit of overreflection theory (e.g., Lindzen and Rosenthal, 1983; Smyth and Peltier, 1989), we seek to understand the physics of this unstable mode through an examination of the radial propagation of a neutral wave field having the same oscillation frequency. At large r, the eigenfunction $\hat{\pi}(r)$ takes the form of the Bessel function $H_2^1(\kappa r)$, with

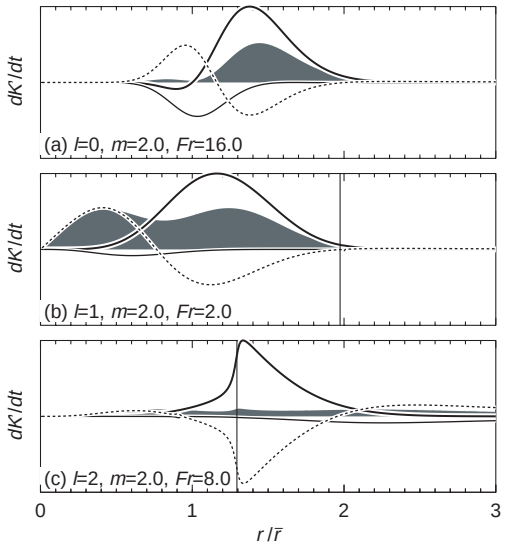

Figure 7. Terms in the perturbation kinetic energy budget (14) for selected unstable modes in the stratified, nonrotating case. The filled curve is the left-hand side of (14), $2\omega_i\langle K'\rangle$. The thick solid curve represents the shear production term, the thin solid curve represents damping by buoyancy, and the dashed curve is the convergence of the radial energy flux. Units on the vertical axis are arbitrary, but the same for all curves. Vertical lines indicate critical radii.

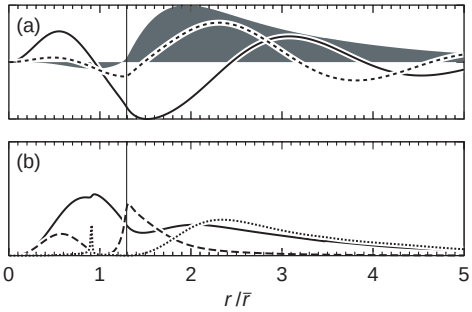

Figure 8. Additional quantities pertaining to the mode shown in Figure 7(c) (l = 2, m = 2.0, Fr = 8.0). (a) The solid and dashed curves correspond to the real and imaginary parts of the eigenfunction $\hat{\pi}$. The filled curve represents the radial energy flux $\langle \hat{\pi}\hat{w} \rangle$. Units on the vertical axis are arbitrary. (b) Individual components of the perturbation kinetic energy. Solid curve: $\frac{1}{2}|\hat{u}|^2$; dashed curve: $\frac{1}{2}|\hat{v}|^2$; dotted curve: $\frac{1}{2}|\hat{w}|^2$. Units on the vertical axis are arbitrary, but the same for all curves.

$\kappa = -0.184 + 0.028i$, which describes outgoing radiation (Figure 8(a)). The decrease in wave amplitude with increasing r is due to two factors. First, the cylindrical geometry of the wave causes amplitude to decay in proportion to $r^{-1/2}$. Second, the fact that the wavetrain is forced by an exponentially growing disturbance causes the amplitude to decay exponentially with r, although it still grows exponentially in time at any fixed point. (This exponential decay should not be confused with evanescence, in which wave amplitude is constant in time but decays exponentially with distance.)

At the critical radius (r = 1.3), the tangential velocity amplitude $|\hat{v}|$ exhibits a sharp peak (Figure 8(b)), consistent with the behavior of waves at a critical level in a parallel shear flow. Near the critical radius, perturbation motion is entirely horizontal, i.e., $|\hat{w}| \ll |\hat{u}|, |\hat{v}|$. In this region the disturbance is analagous to a Rossby wave, in the sense that the restoring force that permits wave propagation is provided by the background vorticity gradient. Outside the critical radius, the disturbance velocity becomes primarily vertical, consistent with radiating gravity waves. Inside the critical radius, $|\hat{w}|$ also becomes large, exhibiting a sharp peak near r = 0.9. This is a turning radius for radially propagating gravity waves. Inside this radius, the background angular frequency Ω (Figure 2(a)) is large, so that the Doppler-shifted frequency of the disturbance, σ_r, becomes larger in magnitude than N. As a result, gravity waves cannot penetrate into the vortex core, but instead are attenuated inside r = 0.9. Inside this radius, the disturbance motion again becomes primarily horizontal, and the radial energy flux (Figure 8(a)) decays.

In summary, these results suggest the following scenario for the instability at l = 2. Rossby-like waves are emitted from the critical radius, then take on the character of gravity waves as they propagate away from that region. Inward-propagating waves are reflected back toward the critical radius, partly because of the turning radius at r = 0.9 and partly because of the closed geometry of the critical surface, creating conditions conducive to growth via repeated overreflection (e.g., Lindzen and Rosenthal, 1983). Outside the critical radius, gravity waves propagate away from the vortex, reducing instability by removing energy from the vicinity of the critical radius. As the stability boundary at low Fr is approached, this radiative damping effect increases until the growth rate is reduced to zero.

3c. The Effects of Rotation

For this set of calculations, we set N to zero and vary f from zero to large values, both positive and negative. Results are presented in terms of the Rossby number, $Ro = \bar{Z}/f$. (Note that Ro may take either sign.) Modes with m = 0 represent purely two-dimensional motion, and are therefore unaffected by rotation. For nonzero m, however, we expect that all modes will be stabilized for sufficiently small $|Ro|$, in consequence of the Taylor–Proudman theorem. A similar prediction may be made for axisymmetric modes on the basis of Rayleigh's theorem (cf. Section 2c): axisymmetric modes cannot grow for Ro between $-e^2 = -7.39$ and +1.

Figure 9 illustrate the effects of finite Ro on the l = 0, l = 1, and l = 2 modes. As usual, we see that the l = 0 mode is stationary, while the l = 1 and l = 2 modes are oscillatory. As expected, modes having m = 0 are unaffected by rotation, while all other modes are damped as $Ro \to 0$. The prediction of stability for $-e^2 < Ro < 1$ is approximately valid, not only for the l = 0 case for which Rayleigh's theorem holds, but also for the l = 1 case and the l = 2 case at large m.

Figure 9 reveals a marked asymmetry between positive and negative Rossby numbers. On the positive side, all three modes are unstable down to $Ro \sim 2$, and the l = 1 and l = 2 modes are *more* unstable in

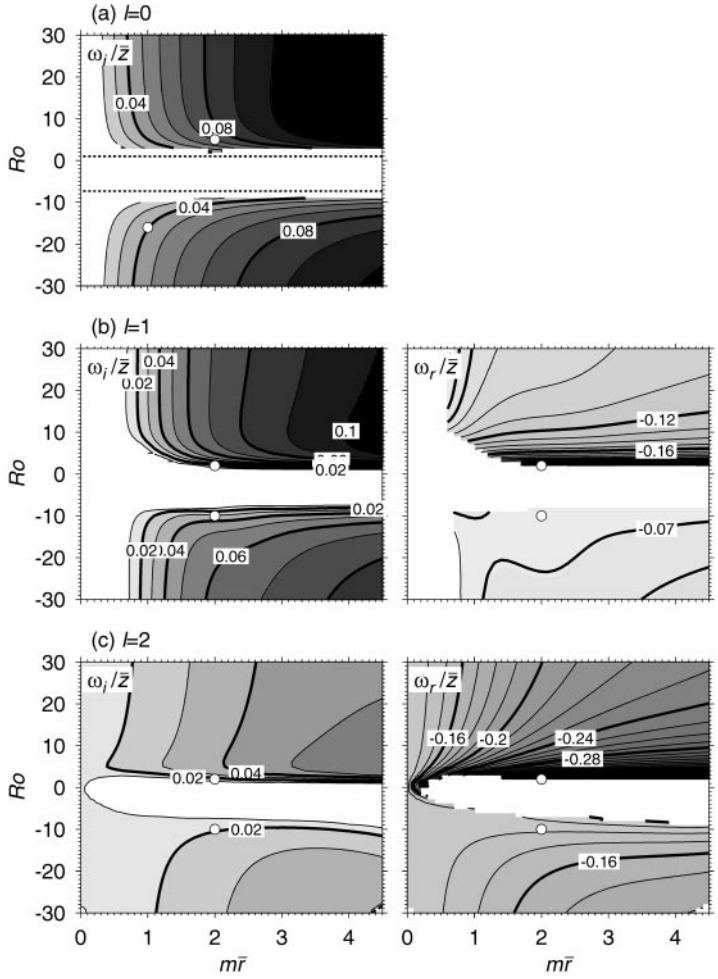

Figure 9. Growth rate versus vertical wave number and Rossby number for the unstratified, rotating case. The limit $|Ro| \to \infty$ corresponds to Figure 3. Dotted lines on (a) indicate the stability boundaries, $Ro = -e^2$ and $Ro = 1$, implied by Rayleigh's criterion. White circles indicate the modes illustrated in Figures 10–12.

the presence of moderate rotation ($Ro \sim 5$–10) than they are in the nonrotating case. In contrast, negative, finite Ro is always stabilizing. The $l = 0$ and $l = 1$ modes are stabilized at $Ro \sim -8$. In the nonrotating case (Figure 3(c)), the $l = 2$ mode has nonzero growth rate at $m = 0$. That mode thus remains unstable, for sufficiently small m, at all Ro.

The aforementioned asymmetry with respect to the sense of the background rotation is reminiscent of the results of Lesieur *et al.* (1991) and Smyth and Peltier (1994). In those studies the background vorticity was sign-definite, so that a clear distinction could be made between cyclonic and anticyclonic vortices. Instability was found to occur preferentially in the anticyclonic case. In the present case, our background flow contains vorticity of both signs: we have a core of strong negative vorticity surrounded by an annulus of weaker positive vorticity, giving a net circulation of zero. Therefore, the distinction between cyclonic and anticyclonic is not clear-cut. If we identify $Ro > 0$ with anticyclonic rotation (i.e., identify the rotation of the vortex by the sign of the strong vorticity at the core), our results are consistent with the previous findings, i.e., that anticyclonic vortices tend to be more unstable than their cyclonic counterparts.

In addition to the asymmetry in growth rates discussed above, nonstationary modes exhibit a Rossby number asymmetry in oscillation frequency (Figure 9(b) and 9(c), right-hand frames). While all oscillation frequencies are negative (so that every unstable mode has a critical radius), frequencies of unstable modes at positive Ro tend to have a larger magnitude. These frequencies increase rapidly as the stability boundary near $Ro = 1$ is approached from above.

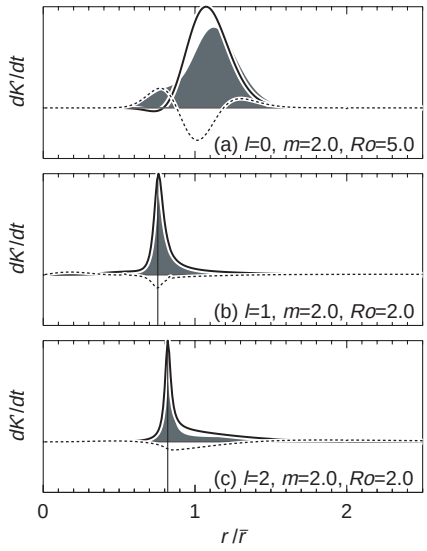

Figure 10. Terms in the perturbation kinetic energy budget (14) for selected unstable modes in the unstratified, rotating case with $Ro > 0$. The filled curve is the left-hand side of (14), $2\omega_i\langle K'\rangle$. The thick solid curve represents the shear production term, and the dashed curve is the convergence of the radial energy flux. Units on the vertical axis are arbitrary, but the same for all curves. Vertical lines indicate critical radii.

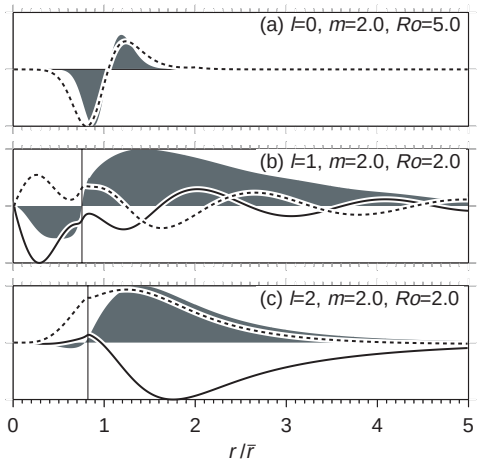

Figure 11. Additional quantities pertaining to the modes shown in Figure 10. (a) The solid and dashed curves correspond to the real and imaginary parts of the eigenfunction $\hat{\pi}$. The filled curve represents the radial energy flux $\langle\hat{\pi}\hat{w}\rangle$. Units on the vertical axis are arbitrary.

Figures 10 and 11 illustrate the radial structures of selected modes close to the stability boundary at positive Ro. The spatial structure of the $l = 0$ mode is similar to that found in the nonrotating case, while the $l = 1$ and $l = 2$ modes have kinetic energy profiles tightly focused near the critical radius (Figure 10). The $l = 1$ mode appears to couple to a field of outgoing inertial-wave radiation (Figure 11(b)). For $Ro < 0$, there is no indication of outgoing radiation (Figure 12). Instead, both the $l = 1$ and $l = 2$ modes exhibit enhanced amplitudes in the interior of the vortex.

In summary, the "ultraviolet catastrophe" which is observed in the nonrotating case is damped in a range of Rossby numbers which extends approximately from $Ro = -e^2$ to $Ro = 1$. Vortices in this range are expected to exhibit weak external instability, with $l = 2$. In the next section we will see how internal modes at small $|Ro|$ may be destabilized by stratification.

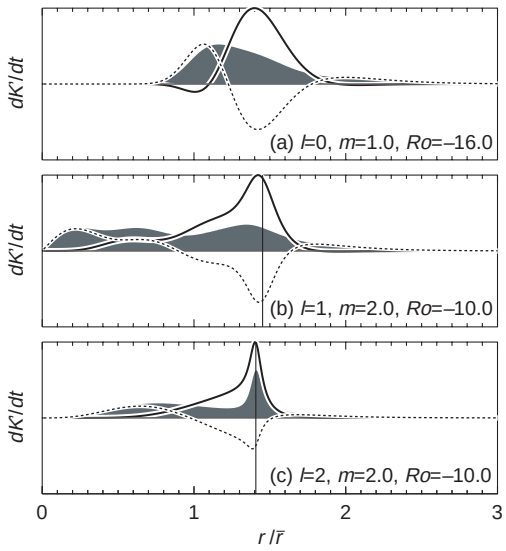

Figure 12. Terms in the perturbation kinetic energy budget (14) for selected unstable modes in the unstratified, rotating case with $Ro < 0$. The filled curve is the left-hand side of (14), $2\omega_i\langle K'\rangle$. The thick solid curve represents the shear production term, and the dashed curve is the convergence of the radial energy flux. Units on the vertical axis are arbitrary, but the same for all curves. Vertical lines indicate critical radii.

3d. The Combined Effects of Stratification and Rotation

In the presence of density stratification, the Taylor–Proudman theorem is no longer applicable, hence instability may persist as $Ro \to 0$ (i.e., in the quasi-geostrophic limit). Using an explicitly quasi-geostrophic model, GM86 found that instability is limited to a band of vertical wave numbers whose upper limit is of order $|N/f|$. This is consistent with the common result that quasi-geostrophic flow features tend to exhibit aspect ratios of order $|f/N|$. The UVC which we have observed at $f = N = 0$ is inconsistent with this scenario, and we therefore expect that modes having large vertical wave numbers will be damped as $Ro \to 0$, as was found in the unstratified case.

We begin by investigating the case in which the inertial frequency and the buoyancy frequency are equal. In Figure 13(a), we see that the $l = 0$ mode is stable for sufficiently small $|Ro|$. The $l = 1$ mode is destabilized at small $|Ro|$ and $m \sim O(1)$, as was found by GM86. (Figure 1 of GM86 corresponds to the cross section

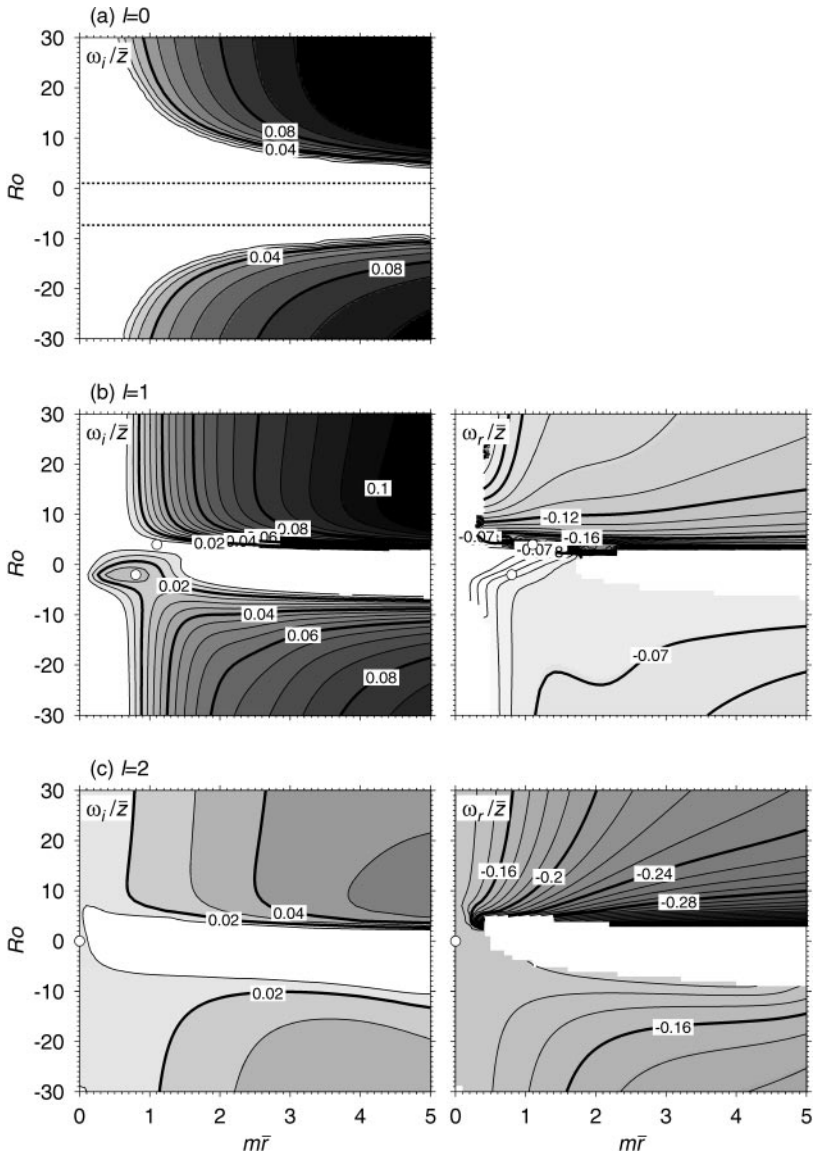

Figure 13. Growth rate versus vertical wave number and Rossby number for the stratified, rotating case $|f|/N = 1$. The limit $|Ro| \to \infty$ corresponds to Figure 3. Dotted lines on (a) indicate the stability boundaries, $Ro = -e^2$ and $Ro = 1$, implied by Rayleigh's criterion. White circles indicate the modes illustrated in Figure 14.

Ro = 0 of our Figure 13(b).) This is evidently a stratification effect: the l = 1 mode in unstratified flow is stable at small Ro (Figure 9(b)), but is unstable in the small-Fr limit (which coincides with the small-Ro limit in this case). In the case l = 2 (Figure 13(c)), a small band of modes having $m \neq 0$ remains unstable in the presence of rotation and stratification. Larger values of m are stable at sufficiently small $|Ro|$.

The results shown in Figure 13 constitute the major point of this paper. To summarize, we find two distinct regimes of instability: scale-selective instability (cf. Figure 1(a)) at small $|Ro|$, and UVC (cf. Figure 1(b)) at larger $|Ro|$. The transition between the two regimes is sharp, and coincides rather closely with the Rossby numbers at which Rayleigh's theorem predicts centrifugal instability (dotted lines in Figure 13(a)). The scale-selective instability has a weak, external component at l = 2 and a stronger, internal component at l = 1. As Ro is increased into the UVC regime, l = 1 and l = 2 modes become unstable first, but l = 0 dominates as $|Ro|$ becomes large.

Selected eigenmodes for the case $f = N \neq 0$ are displayed in Figure 14. All of the modes illustrated exhibit the broad radial support that is characteristic of the stratified case (cf. Figure 7) and rotating flow with $Ro < 0$ (cf. Figure 12). Note also the sharp spikes in the kinetic energy profile for Ro = 4, m = 1.1. At no point is radiative behavior observed at large r. This is expected, since $|f| = N$, and κ is therefore imaginary.

The condition $|f/N| = 10^{-2}$ is characteristic of many geophysical flow regimes. The problem becomes stiff at these extreme parameter values, and our shooting code often has difficulty in finding unstable modes which are, in fact, present. As a result, we do not explore this case in detail here. For the present purposes, it suffices to show that the qualitative stability characteristics; i.e., the transition between scale-selective and UVC behavior, occur in this case as well as in the numerically less-demanding case $|f/N|$ = 1.

Results for $|f/N| = 10^{-2}$ are shown in Figure 15. Our shooting code has not found any unstable modes at l = 0; this may be an artifact of numerical instability. The growth rate and frequency of the l = 1 mode for the case $|f/N|$ = 0.01 are shown in Figure 15(a). The horizontal axis now represents the scaled vertical wave number $Fr/Ro = m\bar{r}|f/N|$. As was found in the case $|f/N|$ = 1, the UVC disappears in a band of Rossby numbers that coincides roughly with the regime of centrifugal stability. In that regime, instability is restricted to vertical wave numbers such that $m\bar{r}|f/N| \sim O(1)$, as expected on the basis of quasi-geostrophic theory. At l = 2, scale-selective instability is once again external (Figure 15(b)).

Tests done at different values of the ratio $|f/N|$ indicate that the results given here are nearly independent of $|f/N|$, provided that $|f/N| \ll 1$.

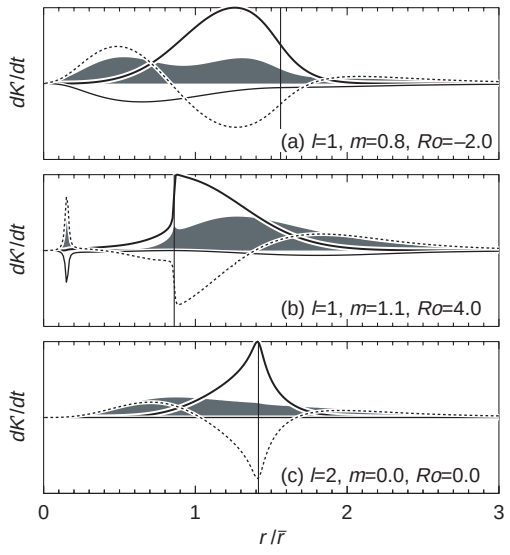

Figure 14. Terms in the perturbation kinetic energy budget (14) for selected unstable modes in the stratified, rotating case with $|f|/N$ = 1. The filled curve is the left-hand side of (14), $2\omega_i\langle K'\rangle$. The thick, solid curve represents the shear production term, the thin solid curve represents damping by buoyancy, and the dashed curve is the convergence of the radial energy flux. Units on the vertical axis are arbitrary, but the same for all curves. Vertical lines indicate critical radii.

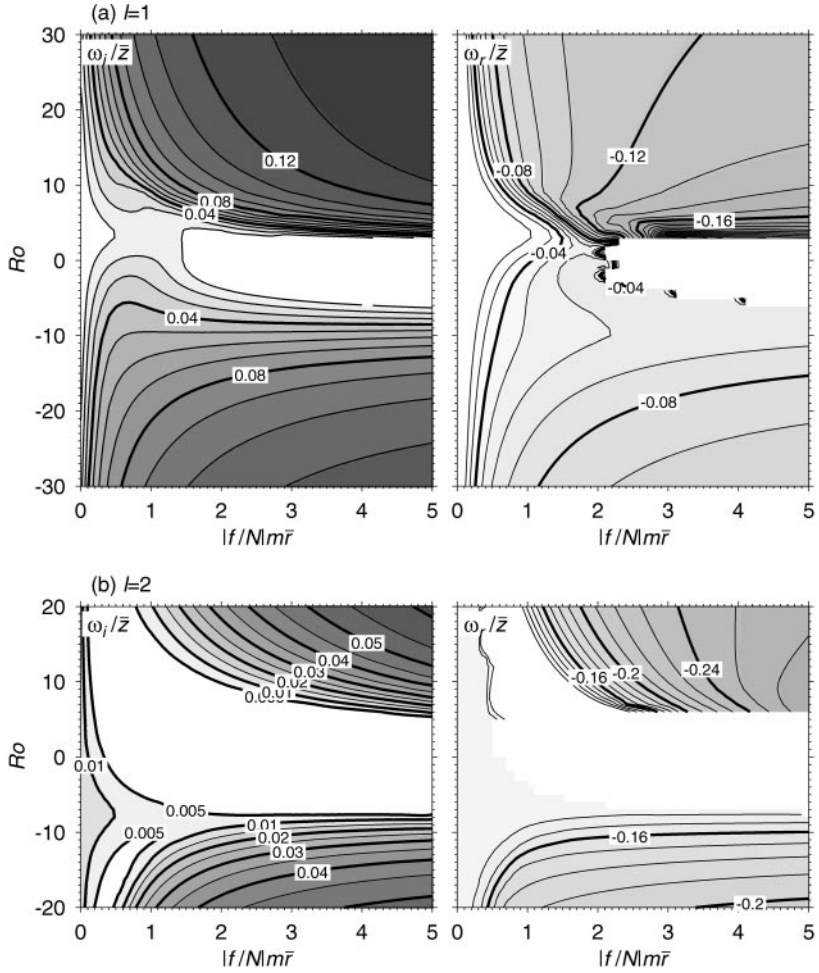

Figure 15. Growth rate versus vertical wave number and Rossby number for the stratified, rotating case $|f|/N = 0.01$.

4. Summary

We have examined the effects of background rotation and stratification upon the normal-mode stability characteristics of the axisymmetric, barotropic vortex described by (16). We have seen how the combined effects of rotation and stratification effect the transition between balanced and UVC behavior. Our discussion has been limited to the linear, inviscid case. Nonlinearity and viscosity are also expected to play important roles. Note, however, that the qualitative features of the transition illustrated in Figure 1, in which both viscosity and nonlinearity are present, are consistent with those predicted in the present analyses. This suggests that rotation and stratification are indeed the dominant factors controlling the transition in stability characteristics.

In the unstratified case, the most unstable mode is axisymmetric ($l = 0$) and is focused in an annulus whose inner radius is 1, the radius at which the centrifugal stability function becomes negative. This instability is stationary, and grows fastest at large vertical wave numbers, suggesting a direct transfer of energy to the dissipation range. The $l = 1$ and $l = 2$ modes are also unstable. Growth rates increase monotonically with increasing m, but are bounded by the Rayleigh criterion (19). It appears that this upper bound is achieved at $m \to \infty$.

In a strongly stratified, nonrotating environment, instability occurs primarily via the UVC at $l = 1$, which is damped as $Fr \to 0$, and the external $l = 2$ mode, which is not. Internal $l = 2$ modes may induce emission of gravity wave radiation from the vortex region. In a rotating, unstratified flow, the UVC is damped in a range of Rossby numbers which extends approximately from $Ro = -e^2$ to $Ro = 1$, the region of centrifugal stability.

Vortices in this range are expected to exhibit weak external instability with $l = 2$, possibly accompanied by inertial wave radiation at $l = 1$.

In the presence of rotation plus stratification, there exists a band of Rossby numbers within which the predictions of quasi-geostrophic theory remain qualitatively valid. Specifically, instability is restricted to a band of vertical wave numbers such that $m\bar{r} \sim |N/f|$. We therefore expect the columnar vortex to break up into three-dimensional vortices having aspect ratios of order $|f/N|\bar{r}$. For the vortex profile presently under consideration, this regime is bounded approximately by the centrifugal stability limits $Ro = -e^2$ and $Ro = 1$. Outside this regime, instability extends to arbitrarily large vertical wave numbers, as is the case when $f = N = 0$. In the latter regime, one expects that the vortex will rapidly disintegrate (c.f. Figure 1(b)). Thus, the quasi-geostrophic approximation is qualitatively valid well beyond its formal region of validity, $|Ro| \ll 1$. When the threshold is crossed, however, the result is a dramatic change in the flow evolution.

Acknowledgement

This work was supported by the National Science Foundation (ATM-9617967).

References

Bartello, P., 1995: Geostrophic adjustment and inverse cascades in rotating stratified turbulence. *J. Atmospheric Sci.* **52**, 4410–4428.

Drazin, P.G. and W.H. Reid, 1981: *Hydrodynamic Stability*. Cambridge University Press, Cambridge, 527pp.

Flatau, M. and D.E. Stevens, 1989: Barotropic and inertial instabilities in the hurricane outflow layer. *Geophys. Astrophys. Fluid Dynamics* **47**, 1–18.

Gage, K.S. and C.G. Nastrom, 1986: Theoretical interpretation of atmospheric wave number spectra of wind and temperature observed by commercial aircraft during GASP. *J. Atmospheric Sci.* **43**, 729–740.

Gent, P.R. and J.C. McWilliams, 1986: The instability of barotropic circular vortices. *Geophys. Astrophys. Fluid Dynamics* **35**, 209–233.

Gill, A.W. and G.E. Sneddon, 1995: Complex mapped matrix methods in hydrodynamic stability problems. *J. Comput. Phys.* **122**, 13–24.

Gill, A.W., G.E. Sneddon and R.J. Hosking, 1993: Matrix methods in barotropic stability analysis. *Geophys. Astrophys. Fluid Dynamics* **72**, 57–69.

Hazel, P., 1972: Numerical studies of the stability of inviscid parallel shear flows. *J. Fluid Mech.* **51**, 39–62.

Kloosterzeil, R.C., and G.J.E. van Heijst, 1991: An experimental study of unstable barotropic vortices in a rotating fluid. *F. Fluid Mech.* **223**, 1–24.

Lesieur, M., S. Yanase, and O. Metais, 1991: Stabilizing and destabilizing effects of a solid body rotation on quasi-two-dimensional shear layers. *Phys. Fluids A* **3**, 403–407.

Lindzen, R.S., and A.J. Rosenthal, 1983: Instability in a stratified fluid having one critical level. Part III: Kelvin–Helmholtz instabilities as overreflected waves. *J. Atmospheric Sci.* **40**, 530–542.

McWilliams, J.C., 1985: Submesoscale coherent vortices in the ocean. *Rev. Geophysics* **23**(2), 165–182.

Peng, M.S., and R.T. Williams, 1991: Stability analysis of barotropic vortices. *Geophys. Astrophys. Fluid Dynamics* **58**, 263–283.

Smyth, W.D., and W.R. Peltier 1989: The transition between Kelvin–Helmholtz and Holmbøe instability: An investigation of the overreflection hypothesis. *J. Atmospheric Sci.* **47**, 3698–3720.

Smyth, W.D., and W.R. Peltier 1994: Three-dimensionalization of barotropic vortices on the f-plane. *J. Fluid Mech.* **265**, 25–64.

Vincent, A., and M. Meneguzzi, 1991: The spatial structure and statistical properties of homogeneous turbulence. *J. Fluid Mech.* **225**, 1–20.

Weber, H.C., and R.K. Smith, 1993: The stability of barotropic vortices: implications for tropical cyclone motion. *Geophys. Astrophys. Fluid Dynamics* **70**, 1–30.

Willoughby, H.E., 1988: Linear motion of a shallow-water, barotropic vortex. *J. Atmospheric Sci.* **45**(13), 1906–1928.

Willoughby, H.E., 1990: Linear normal modes of a moving, shallow-water barotropic vortex. *J. Atmospheric Sci.* **47**(14), 2141–2148.